Low-Field Memristive Switching in Epitaxially Strained SnS Thin Film

Michael Rohde Mohammadali Razeghi Jean Spiece Gaohang He Alessandra Canetta Valentin Fonck Francisco Molina-Lopez Clement Merckling Pascal Gehring**

Michael Rohde, Mohammadali Razeghi, Dr. Jean Spiece, Valentin Fonck, Alessandra Canetta, Prof. Pascal Gehring
Institute of Condensed Matter and Nanosciences, Université catholique de Louvain (UCLouvain), 1348 Louvain-la-Neuve, Belgium
Email Address: pascal.gehring@uclouvain.be

Michael Rohde, Francisco Molina-Lopez
Department of Material Engineering, KU Leuven, 3001 Leuven, Belgium

Michael Rohde, Dr. Gaohang He, Prof. Clement Merckling
IMEC, 3001 Leuven, Belgium
Email Address: clement.merckling@imec.be

Prof. Pascal Gehring
WEL Research Institute, 1300 Wavre, Belgium

Keywords: *Tin Sulfide, Plasma, Molecular Beam Epitaxy, Thin Film, Memristor, Strain*

The quasi van der Waals (vdW) polarizable semiconductor, tin monosulfide (SnS), holds exceptional potential as a memristor in neuromorphic architectures as well as for sustainable, mechanically flexible and biocompatible photovoltaic and piezoelectric applications. So far, the synthesis of SnS remained limited to flake scale growth or subject to a compromise between substrate interaction and crystal order. In this work, we overcome this limitation by introducing a substrate pre-treatment with reactive sulfur to a hybrid chemical/physical growth method. Our approach achieves the sharply interfaced growth of a textured epitaxial SnS thin film directly on α-Al_2O_3 introducing in-plane strain and centrosymmetry breaking. These films possess stable and programmable memristive switching behaviour with a switching field of 360 V/cm, orders of magnitude lower than in previous studies on SnS. We thus demonstrate the interplay of epitaxially induced strain and symmetry breaking in SnS, paving the way for its thin film scale integration in the next generation of energy efficient and material-level adaptive electronics.

1 Introduction

In a polarizable material, electric dipoles form domains that can be manipulated and stabilized by means of an electric field. By combining information storage and computation in a single device, these materials are of high interest for energy cost efficient switches in non-volatile memory applications or memristors for analog neuromorphic architectures [1, 2].
Meanwhile, research on layered vdW materials has pushed the layer thickness scale down to the 2D limit allowing the exploration of unique physical properties and fabrication prospects [3]. The overlap of these two fields, namely ultra-thin, polarizable and layered materials, holds great promise for multi-functional nano devices as the low dimensionality can introduce inter-coupling of photoelectricity, piezoelectricity, spin polarization and electric polarization[4].
Among the few examples[5, 6, 7], the group-IV monochalcogenide and semiconductor SnS stands out thanks to its high electric response to force, light and temperature [8, 9, 10], as well as its relatively abundant and non-toxic constituents. However, mechanical exfoliation is particularly challenging for SnS due to relatively strong inter-layer coupling sometimes referred to as "weak covalent bonding"[11], hence the term "quasi" vdW. This has motivated the exploration of engineering its thin film properties by bottom-up synthesis routes.
In its most stable form at room temperature, basal plane SnS adopts a layered orthorhombic structure (space group Pnma) with vdW layers parallel to the surface. Traditionally, SnS with an even number of

AB-stacked layers (see Supporting Info, Figure.S1) is centrosymmetric and spontaneous polarization can occur only in the mono- and odd- layered system where centrosymmetry breaking is guaranteed, leading to ferroelectricity[12, 13, 14]. The search to overcome this limitation has led to the discovery of systems where centrosymmetry is instead broken either by an external electric field or by modifications of the SnS structure into AA-type stacking[15, 16]. In principle, such structural alterations can be controlled during epitaxial growth which is sensitive to stress initiated at the substrate interface. So far however, the synthesis on strongly interacting substrates typically yielded relatively disordered films or was accompanied by the formation of an amorphous SnS buffer layer[17, 18, 19].
In this work, we demonstrate centrosymmetry breaking and memristive switching behaviour in ultra thin (18 nm) basal plane textured SnS films grown by a plasma assisted molecular beam epitaxy (PA-MBE) method directly on α-Al_2O_3. This was achieved by adding a reactive sulfur pre-treatment to a hybrid physical/chemical deposition method which has previously been effective for MoS_2 synthesis [20]. We find high crystal quality and strain evidenced by electron diffraction (RHEED), atomic force microscopy (AFM), Raman spectroscopy (Raman), scanning transmission electron microscopy (STEM) and X-ray diffraction (XRD). Using piezoresponse force microscopy (PFM) we show local centro-symmetry breaking and demonstrate in transport measurements, that our films can be switched in a cyclic and memristive manner, exhibiting the lowest switching field for SnS reported to date.

2 Results

Two films (M1 and M2) with different growth strategies are presented in the main text (see Supporting Info, Figure S2 for other films M3 - M6). Schematics of the growth method for M2, which involves a H_2S plasma pretreatment, are shown in **Figure 1** a) and b) (for more detail see "Experimental Section").
The effect of the pre-treatment is apparent in Figure 1 c) and d). Figure 1 c) shows in-situ RHEED images of M1 and M2 along with intensity profiles extracted horizontally across the pattern. In the kinematic approximation [21], the spacing W of diffraction streaks in the RHEED pattern is directly linked to the reciprocal lattice spacing of the crystal by $1/d \propto W$. Taking the known pattern of the Al_2O_3 substrate for in-plane lattice calibration we quantify the streak/spot distance of the SnS patterns and compare with expected values of the SnS lattice parameters. On M1, transmission-like RHEED spots indicate the growth of 3D islands with crystal spacings matching SnS(100) and SnS(102) planes. In contrast, on M2, we obtain intense diffraction streaks showing the growth of 2D layers with spacings matching vertical planes SnS(200) and SnS(110) (see dashed lines in Figure 1 c)).
The difference of growth mode between M1 and M2 is further highlighted by the contrast of surface morphology in AFM images shown in Figure 1 d). On M1, standing grains grow at distinct angles (see Supporting Info, Figure S3) that match the RHEED observations and form a discontinuous 3D film. On M2, a distinctly more continuous thin film of flat grains is formed. On some grains we find spiraling terraces (28 spirals/2μm x 2μm), a feature stemming from screw dislocations that has been linked to inversion symmetry breaking in other layered structures [22].
For chemical and structural characterization we probed M2 by Raman, XRD and STEM. The results are displayed in **Figure 2**.
We fit the Raman spectrum (raw data: solid blue line, fit: dotted black line in Figure 2 a)) with 10 Lorentzian peaks. Four of the most prominent modes at 95.4 cm^{-1}, 185.4 cm^{-1}, 220.8 cm^{-1} and 156.4 cm^{-1} can be attributed to the $A_{g(1-3)}$ and a B_g mode, respectively [14]. The additional peak at 133.6 cm^{-1} (marked by *) can be attributed to an infra red active (but Raman forbidden) B_u mode hinting at centro-symmetry breaking. The Raman spectrum of M1 shows similar characteristics (see Supporting Info, Figure S5) highlighting that their difference is predominantly structural and excluding significant amounts of further Sn-S phases. The observed Raman shift differences of M1 and M2 can be attributed to anisotropic strain differences between the samples (see Supplementary Info, Figure S11 c) for more detail). The additional strain on M2 may be a result of increased interface area with the lattice mismatched substrate or lower grain thickness compared to M1. For further chemical characterization, Figure 2 f) shows EDS

maps along with elemental profiles taken across the z direction. Oxidation is confined to a few nm at the surface after months of storage in ambient conditions and only a small amount of S replacement occurred during lamella extraction and transfer, confirming the excellent chemical stability of the film.
In Figure 2 b)-e) we study the structure in more detail by out-of-plane (OOP) XRD scans and cross sectional STEM. OOP ω-2θ scans reveal SnS(004) and SnS(008) peaks in M1 and M2 showing the presence of basal plane-SnS in both samples. The intensity of the SnS(004) diffraction peak is about 25 times higher in the H_2S pretreated M2, confirming the significant increase in crystallographic order compared to the non-pretreated M1. In our ω-scan (rocking curve) at the SnS(004) angle (ω-$2\theta = 15.68°$), we find an additional superposed peak with low full width half maximum (FWHM) of 0.15° showing a high degree of crystallographic order. This peak is associated with $c/4$ lattice spacing in the crystal, i.e. the vertical spacing of Sn atoms in basal plane SnS layers. Mapping out diffraction in a reciprocal space map (RSM), we find faint peaks at (p_1 at (ω-offset, 2θ) = $(2.2°, 34.7°)$ and p_2 $(1.5°, 45.5°)$) on both M1 and M2 (see Supporting Info, Figure S5), possibly due to minor amounts of non-basal plane SnS or SnS_2. In Figure 2 c), we characterize off axis planes SnS(102) and SnS(111) by varying the polar angle χ. Fixing $2\theta = 25.4°$ simultaneously probes SnS(012) and Al_2O_3(012) (marked with *) showing the presence of a defined epitaxial relationship. We observe a small splitting of the SnS(111) diffraction peaks due to the multi-domain nature of the film in combination with the inequality between lattice parameters a and b. The $\Delta\phi_1$ of this splitting as well as $\Delta\phi_2$ between SnS(012) and SnS(111) provide a measure of the ratio a/b according to a simple geometrical consideration (see Supporting Info, Figure S7 for more detail). We find $\Delta\phi_1 = 3.2(4)°$ and $\Delta\phi_2 = 16.7(2)°$ and thus $a/b = 0.942(6)$ and 0.946(6), respectively. Compared to common a/b ratios in literature this value is surprisingly high (Figure 2 d)). In fact, we obtain the best match for SnS at 700 K, close to the growth temperature used for M2 (650 K). Hence, we attribute the a/b ratio to a high temperature variant of SnS intermediate between Pnma and Cmcm formed at growth temperature and remaining stable during cool down.
Here, we study the epitaxial relation and strain in more detail. The annular bright-field (ABF)-STEM image in Figure 2 e) reveals an intimate contact between the AB stacked SnS film and the substrate featuring a dislocation-free, sub-nm interface with a defined epitaxial relation. Notably, this interface is virtually free of an amorphous buffer in contrast to previous SnS films grown on non-vdW substrates [18, 19]. We find $a = 4.045$ $\mathring{A}$, $b = 4.300$ $\mathring{A}$ and $c = 11.290$ $\mathring{A}$ (see Supporting Info, Figure S6), corresponding to a considerable mismatch of a and b relative to 2 x $d_{110}^{Al_2O_3} = 4.82$ $\mathring{A}$ of the substrate by -19.1 % and -12.1 %, respectively.
To study the effect of strain on the materials properties we performed electrical testing on the as-grown films contacted in van der Pauw geometry using Indium spheres (see schematic in **Figure 3** a)). We find a sheet resistivity of 1.97 Ωcm at room temperature. This value is comparable but lower than 5.18 Ωcm measured parallel to layers in single crystal SnS[23].
Figure 3 a) shows the temperature dependence of the sheet conductivity σ of the basal plane SnS films. Using an Arrhenius model $\sigma(T) = \sigma_0 \exp(-E_a/k_B T)$, where k_B is the Boltzmann constant and where the activation energy is $E_a = E_g/2$ for intrinsic semiconductors, we can estimate a band gap of $E_g =$ 0.38 eV. This value is lower than 1 eV previously found for SnS films [24]. As discussed above (see Figure 1 d)), the present SnS film appears to be an epitaxially stabilized intermediate between its low temperature Pnma and high temperature Cmcm phase. Recent studies have found that the transition between these two phases corresponds to a significant and monotonous reduction of optical band gap as the crystal approaches the SnS Cmcm phase at high pressures[25]. This sizeable effect further begs the question whether the amount of stabilized structural distortion is sufficient to affect the centro-symmetry and polarization of the SnS crystal. Such an effect has been predicted for related chalcogenides[26]. An indication of such an effect in the present film has been found in Raman as mentined above (see Figure2 a)).
Furthermore, centro-symmetry breaking is a necessary condition for the piezoelectric effect and can thus be measured by PFM. In conventional PFM, an electric field perpendicular to the film is applied between a back electrode and a conductive AFM tip (out-of-plane configuration) and the piezoelectric response is measured by the deflection of that same AFM tip. Here, to stimulate the in-plane polarization of SnS, we apply the electric field laterally (in-plane configuration in Figure 3 b)) using manually placed

In contacts. This method comes with the added benefit of decoupling the AFM probe from the applied electric field and has previously been adopted to probe the piezoelectric response of MoS_2[27].
In Figure 3 c), we show the PFM amplitude and phase signal recorded in the center of the film as a function of the DC voltage (added to an AC voltage used for lock-in demodulation, see Methods) applied to the device. We observe hysteretic behavior in both, the amplitude and phase signal, and a maximum PFM response at -7 V. We then scan across the edge of the patterned film as shown in the topographic image in Figure 3 d) which enables a direct comparison with the non-piezoelectric substrate. In Figure 3 e) we show the resulting maps of the vertical and lateral PFM amplitude and phase recorded at -7 V DC bias. We find strong PFM signal on the entire SnS film and no signal beyond lockin noise on the substrate. Here, "vertical" and "lateral" refer to the y and x deflection recorded on the laser detector. We attribute the higher signal-to-noise ratio of the lateral image to the lower stiffness associated to the lateral movement of the probe. The average phase on the film is 56(20)° and -80(130)° for the vertical and lateral measurement, respectively (standard deviation across full area is noted in brackets). This difference contains contributions from probing orthogonal directions of deformation as well as contributions from differing probe-surface interactions associated to the x and y deflection.
These results prove local non-centrosymmetry and open up the potential for the appearance of polarization and memristive behavior in M2[12]. **Figure 4** shows transport data recorded on the same device as in Figure 3 a)-d). We observed a sizable impact of microscope illumination in favor of both, overall conductance and the switching behavior in M2 (see Supporting Info, Figure S8). All transport measurements presented in Figure 4 have been recorded under that same illumination. In Figure 4 a) we show the current density of the SnS device as a function of increasing electric field range E_{max}. A linear background was fitted to the highest range sweeps and subtracted from the raw data for clarity (see Supporting Information, Figure S8 for more details). We observe loops opening up as E_{max} is incrementally increased up to 770 V/cm. We observe partial loops varying continuously as a function of the applied field range. The overall resistance ρ also varies continuously with E_{max} until saturation is reached at E_{max} = 600 V/cm.
We quantified the variation of ρ in Figure 4 a) by extracting current values from IV back traces at a fixed reading voltage E_{read}, a process akin to memristor writing and reading cycles. Figure 4 b) shows the variation of this reading resistivity ρ_{read} in function of the IV sweep range E_{max} (i.e. writing fields). ρ_{read} is smallest at the minimum writing field, $\rho_{read,min} = 6.5\ \Omega cm$ at E_{max} = 270 V/cm, and reaches up to $\rho_{read,max} = 12.4\ \Omega cm$ at E_{max} = 770 V/cm, a programmable variation of 91 %. Values for ρ_{read} include the linear background that has been subtracted in Figure 4 a). In Figure 4 d) we recorded 100 consecutive traces within the saturated range (E_{max} >600 V/cm) and consistently reproduce the same current peak amplitude and field corresponding to a switching field of 360 V/cm. Following the measurement scheme in Figure 4 e) we conducted repeated double wave measurements (DWM) [28]. This method probes non-volatile contributions by subtracting (possibly non-linear) dielectric contributions measured by a follow up secondary sweep. Accordingly, in Figure 4 e)(i-ii) we plot both, primary and secondary sweeps for both polarities, where a polynomial fit to the secondary waves (i.e. dielectric background) have been subtracted. The primary sweep (orange) is clearly distinguished from the secondary sweep (blue) by a pronounced current peak for both electric field polarities. The amplitude in the DWM is consistent with the amplitude observed in Figure 4 d) showing the non-volatility of the memristive state[15, 28]. In Figure 4 f), we show a simultaneous measurement of current and accumulated charge Q (conductive background contributions have been subtracted, see Supporting Info Figure S9). The hysteresis is a result of the conductance switching during the voltage sweep.

3 Discussion

Growth facilitated strain engineering of vdW thin films poses the challenge of manipulating epitaxial stress while maintaining crystal order. The desired stress can be induced by reactive conditions, such as the choice of a reactive substrate or the involvement of reactive gases, but these may also result in disordered films. Especially for vdW materials, growth mechanisms are favored at the edges of layers which

can lead to standing grain type growth on reactive substrates[17]. Our results on M1 confirm this trend for SnS. However, we demonstrate that this hurdle can be overcome with the pre-treatment on M2 and the resulting strained film has a defined epitaxial relation and a sharp interface with the substrate. The exact mechanism of the pre-treatment remains open for further investigation. We compared AFM images of a pristine and pre-treated α-Al_2O_3(001) substrate (see Supplementary Info, Figure S10) which shows the appearance of smooth but amorphous features on the substrate surface. This could be due to the formation of Al-S phases at high temperatures[29]. We found that even sub-nm resolution characterization by STEM was unable to identify such phases, perhaps due to re-oxidization of Al, making the characterization of such a mechanism highly challenging. The red shift for $A_{g(2)}$ and B_g in our Raman spectrum has previously been linked to increased lattice parameters a and c and decreased b which matches our observations in XRD and STEM in M2[30]. Based on lattice constants reported in literature[31, 32] ($a = 3.98$ $\mathring{A}$, $b = 4.33$ $\mathring{A}$ and $c = 11.20$ $\mathring{A}$) and our STEM measurements ($a = 4.045$ $\mathring{A}$, $b = 4.300$ $\mathring{A}$ and $c = 11.290$ $\mathring{A}$), we obtain tensile strain of 1.6% and 0.8% for a and c, respectively, and compressive strain of 0.7% for b. A high temperature SnS structure appears to have formed during the high temperature growth and been supported by the substrate during cool down to room temperature, explaining the present a/b ratio. This hypothesis is further supported by a/b ratios found from XRD pole figures, the observation of a reduced band gap[25], our findings of a mismatched but sharp film-substrate interface, the strong inter-layer coupling unique to SnS and previous observations of strain stabilization in SnS on Sn-buffered MgO [33]. Comparable deformations of the lattice are associated to the difference between AB- and AA stacked SnS in previous studies (0.3%, 0.3% and 1.3% for a, b and c, respectively)[31], where the largest strain lies in the c direction as opposed to the a direction in the present study. Interestingly, we found that anisotropic strain in a direction can be maintained over >15 nm, the critical thickness found for the c direction. This likewise appears to lead to centro-symmetry breaking and memristive behavior.

We found a switching field of 360 V/cm, orders of magnitude below the previously reported 25 kV/cm in up to 9 layer, AA-stacked SnS, 10.7 kV/cm for bulk SnS with gate induced non-centrosymmetry[15, 16] and reported values of coercive fields in ferroelectric materials (see Fig.4g))[34, 35, 36].

In parts this can be attributed to the larger thickness d which scales down the switching field by $E_c \propto d^{-2/3}$ according to the Janovec-Kay Dunn model and by lowering the depolarization field and contributions from non-switchable interfaces which become most pronounced in the few nm regime[36, 34]. Strain can have the additional effect of lowering E_c which has previously lead to low-voltage-switching in $BaTiO_3$ and can tune ferroelectric behavior in TMDs[37, 12]. Furthermore, our findings attribute a key role to the exposure to light (see Supplementary Info, Figure S8) which might drive phase instability and mobility of ferroelectric domains. Another clue is given by the observation of a lack of macroscopic ferroelectric domains within the resolution in our PFM maps (Figure 3). The formation of nano-domains due to the strain in the present SnS thin film is consistent with the significantly decreased switching fields observed in this study. This effect is analogous to lower coercive fields in disordered ferromagnets and has recently been discussed for ferroelectrics[38]. We show that under these conditions the conductivity of the SnS film is both programmable by applied electric field and stable once the field is removed. The link between partial ferroelectric switching and bulk conductivity in the strained SnS system may be caused by the interaction between polarization and Schottky barriers, band structure, defects or counter-polarized domains and would be an interesting aspect in further studies.

As previously demonstrated for polycrystalline SnS films [39], E-field induced partial resistance switching of SnS as shown in Figure 4 a) and b) offers a way for neuromorphic programming in synaptic devices. Furthermore, due to the particularly low switching field, SnS has high potential in low energy cost applications. Finally, due to the photosensitivity of SnS, light exposure could provide an additional tuning parameter for the development of remote, optically controlled switching applications[40].

4 Conclusion

In summary, we explored a physical/chemical hybrid synthesis method for growing epitaxial SnS under high stress conditions. We identified H_2S plasma pre-treatment as an effective and crucial step for the basal plane growth on the lattice mismatched α-Al_2O_3 substrate demonstrating its key role for epitaxial strain induced tuning of the SnS structure. The resulting strained thin film shows multiple signs of centro-symmetry breaking together with reproducible and programmable resistance switching at an ultra-low switching field of 360 V/cm under illumination, making it a readily applicable quasi vdW polarizable material with great potential for scalable and energy-efficient memristor applications.

5 Experimental Section

Film Growth:
Growth strategies with different pre-treatment have been adopted for M1 and M2. The pre-treatment of M1 involved outgassing at 400°C for 10 min. The pre-treatment of M2 involved 10 min of exposure to H_2S plasma (radio frequency power of 600 W) at elevated substrate temperature (T set point of 750 °C) which resulted in a chamber pressure of 10^{-5} Torr. We find that the film's growth mode sensitively depends on T during this step, where executing the pre-treatment with a substrate temperature of T = 600 °C reduces the basal plane growth of the grains significantly (see sample M4 in Supporting Info, Figure S2). After their respective pre-treatments, both samples were left to cool to growth temperature (370 °C for M1 and 350 °C for M2). Both films were grown on commercial 2" c-plane α-Al_2O_3 wafers by simultaneous exposure to 100 W H_2S plasma and Sn vapor from an effusion cell kept at 1130 °C. The base pressure of the growth chamber was 10^{-9} Torr. Chemical uniformity of M2 was confirmed by comparing Raman and X-ray photoelectron spectroscopy (XPS) spectra in the central region and edge region of the wafer (see Figure S11).

Device Fabrication:
The device for transport and PFM was prepared by standard optical lithography including a Ar plasma dry etch step for removing the SnS film. The needle contacts where manually placed using In melt.

Structural Characterization and Transport:
RHEED electrons with 15 kV acceleration voltage where directed at the sample surface at an incident angle of 2-3°. AFM images where recorded with a Dimension Edge tool (Bruker) operated in tapping mode. Raman spectra where recorded with LabRAM HR system (Horiba Scientific), a excitation wavelength of 633nm and a 600 grating. XRD scans were performed with XRD diffractometer X'pert (Malvern Panalytical) operated at 45 kV/40 mA acceleration/filament current. Calibration was done on the Al_2O_3(006) peak of the substrate. Incident X-rays had Cu-Kα energy of 8 keV and spectra where recorded with a PIXcel as point detector. TEM samples were prepared by covering the sample with Spin-on-Carbon by drop casting followed by Pt deposition (5 kV, then 30 kV) and side thinning lift out (Helios, TFS). TEM, STEM and EDS maps were recorded using a Thermo Fisher G2 60-300 Titan^3 operated at 200 kV. PFM signal was recorded by lockin technique using HF2LI (Zurich Instruments). We applied a modulated voltage (-7 V DC + 6 V AC) in an in-plane configuration, fully polarizing the film. Vertical and lateral deformations were measured using the lock-in technique on the x and y deflection of an AFM probe operated in contact mode. The driving frequency was 1 kHz which is off resonance for the used probe. Transport measurements were performed with an externally controlled Keithley 2450 sourcemeter and a Keithley 6514 electrometer. Voltages V and currents I were converted to electric field E and current density j using the dimensions of the device l x w x t = 130 μm x 50 μm x 18 nm and E=V/l, j=I/A, A=w x t. This should slightly overestimate the field acting on the SnS film due to the voltage drop at the contact interfaces.

Supporting Information
Supporting Information is available from the Wiley Online Library or from the author.

Acknowledgments
The authors knowledge Chris Drijbooms and Olivier Richard for performing the TEM measurements and Anja Vanleenhove and Thierry Conard for performing XPS measurements. Furthermore, the authors acknowledge financial support from the F.R.S.-FNRS of Belgium (FNRS-CQ-1.C044.21-SMARD, FNRS-CDR-J.0068.21-SMARD, FNRS-MIS-F.4523.22-TopoBrain, FNRS-PDR-T.0128.24-ART-MULTI, FNRS-CR-1.B.463.22-MouleFrits, FNRS-FRIA-1.E092.23-TOTEM, FNRS-GEQ-UG.0102.2F-Attohmics), from the EU (ERC-StG-10104144-MOUNTAIN), from the Federation Wallonie-Bruxelles through the ARC Grant No. 21/26-116, and from the FWO and FRS-FNRS under the Excellence of Science (EOS) programme (40007563-CONNECT) and by KU Leuven Internal Funds Global PhD Partnerships with UC Louvain (GPUCL/21/021).

References

[1] N. Setter, D. Damjanovic, L. Eng, G. Fox, S. Gevorgian, S. Hong, A. Kingon, H. Kohlstedt, N. Park, G. Stephenson, I. Stolitchnov, A. K. Taganstev, D. V. Taylor, T. Yamada, S. Streiffer, *Journal of applied physics* **2006**, *100*, 5.

[2] W. Chen, L. Song, S. Wang, Z. Zhang, G. Wang, G. Hu, S. Gao, *Advanced Electronic Materials* **2023**, *9*, 2 2200833.

[3] K. S. Novoselov, A. Mishchenko, A. Carvalho, A. Castro Neto, *Science* **2016**, *353*, 6298 aac9439.

[4] L. Qi, S. Ruan, Y.-J. Zeng, *Advanced Materials* **2021**, *33*, 13 2005098.

[5] C. Zheng, L. Yu, L. Zhu, J. L. Collins, D. Kim, Y. Lou, C. Xu, M. Li, Z. Wei, Y. Zhang, M. T. Edmonds, S. Li, J. Seidel, Y. Zhu, J. Z. Liu, W.-X. Tang, M. S. Fuhrer, *Science advances* **2018**, *4*, 7 eaar7720.

[6] A. Lipatov, P. Chaudhary, Z. Guan, H. Lu, G. Li, O. Crégut, K. D. Dorkenoo, R. Proksch, S. Cherifi-Hertel, D.-F. Shao, E. Y. Tsymbal, J. Íñiguez, A. Sinitskii, A. Gruverman, *npj 2D Materials and Applications* **2022**, *6*, 1 18.

[7] J. Huo, L. Li, H. Zheng, J. Gao, T. T. T. Tun, H. Xiang, K.-W. Ang, *ACS nano* **2024**.

[8] H. Khan, N. Mahmood, A. Zavabeti, A. Elbourne, M. A. Rahman, B. Y. Zhang, V. Krishnamurthi, P. Atkin, M. B. Ghasemian, J. Yang, G. Zheng, A. R. Ravindran, S. Walia, L. Wang, S. P. Russo, T. Daeneke, Y. Li, K. Kalantar-Zadeh, *Nature communications* **2020**, *11*, 1 3449.

[9] J. A. Andrade-Arvizu, M. Courel-Piedrahita, O. Vigil-Galán, *Journal of Materials Science: Materials in Electronics* **2015**, *26* 4541.

[10] W. He, D. Wang, J.-F. Dong, Y. Qiu, L. Fu, Y. Feng, Y. Hao, G. Wang, J. Wang, C. Liu, J.-F. Li, J. He, L.-D. Zhao, *Journal of Materials Chemistry A* **2018**, *6*, 21 10048.

[11] R. Banai, M. Horn, J. Brownson, *Solar energy materials and solar cells* **2016**, *150* 112.

[12] R. Fei, W. Kang, L. Yang, *Physical review letters* **2016**, *117*, 9 097601.

[13] H. Wang, X. Qian, *2D Materials* **2017**, *4*, 1 015042.

[14] P. Sutter, H. Komsa, H. Lu, A. Gruverman, E. Sutter, *Nano Today* **2021**, *37* 101082.

[15] N. Higashitarumizu, H. Kawamoto, C.-J. Lee, B.-H. Lin, F.-H. Chu, I. Yonemori, T. Nishimura, K. Wakabayashi, W.-H. Chang, K. Nagashio, *Nature communications* **2020**, *11*, 1 2428.

[16] Y. Bao, P. Song, Y. Liu, Z. Chen, M. Zhu, I. Abdelwahab, J. Su, W. Fu, X. Chi, W. Yu, W. Liu, X. Zhao, Q.-H. Xu, M. Yang, K. P. Loh, *Nano letters* **2019**, *19*, 8 5109.

[17] P. Sutter, E. Sutter, *ACS Applied Nano Materials* **2018**, *1*, 6 3026.

[18] M. Devika, N. Koteeswara Reddy, M. Prashantha, K. Ramesh, S. Venkatramana Reddy, Y. Hahn, K. Gunasekhar, *physica status solidi (a)* **2010**, *207*, 8 1864.

[19] K. K. Leung, W. Wang, H. Shu, Y. Y. Hui, S. Wang, P. W. Fong, F. Ding, S. P. Lau, C.-h. Lam, C. Surya, *Crystal growth & design* **2013**, *13*, 11 4755.

[20] S. El Kazzi, W. Mortelmans, T. Nuytten, J. Meersschaut, P. Carolan, L. Landeloos, T. Conard, I. Radu, M. Heyns, C. Merckling, *Journal of Applied Physics* **2018**, *123*, 13.

[21] M. A. Hafez, M. K. Zayed, H. E. Elsayed-Ali, *Micron* **2022**, *159* 103286.

[22] L. Zhang, K. Liu, A. B. Wong, J. Kim, X. Hong, C. Liu, T. Cao, S. G. Louie, F. Wang, P. Yang, *Nano letters* **2014**, *14*, 11 6418.

[23] M. Nassary, *Journal of Alloys and Compounds* **2005**, *398*, 1-2 21.

[24] N. Sato, M. Ichimura, E. Arai, Y. Yamazaki, *Solar energy materials and solar cells* **2005**, *85*, 2 153.

[25] Y. Shi, M. Wu, K. Wang, J. Luo, H. Liu, Y. Wu, H. Huang, *Physical Review B* **2025**, *111*, 17 174107.

[26] T. Xu, X. Wang, J. Mai, J. Zhang, J. Wang, T.-Y. Zhang, *Advanced Electronic Materials* **2020**, *6*, 1 1900932.

[27] S. K. Kim, R. Bhatia, T.-H. Kim, D. Seol, J. H. Kim, H. Kim, W. Seung, Y. Kim, Y. H. Lee, S.-W. Kim, *Nano Energy* **2016**, *22* 483.

[28] M. Fukunaga, Y. Noda, *Journal of the Physical Society of Japan* **2008**, *77*, 6 064706.

[29] Y. Xiao, D. V. D. Plas, J. Soons, S. Lans, A. V. Sandwijk, M. Reuter, *Canadian metallurgical quarterly* **2004**, *43*, 2 283.

[30] M. Guc, J. Andrade-Arvizu, I. Y. Ahmet, F. Oliva, M. Placidi, X. Alcobé, E. Saucedo, A. Pérez-Rodríguez, A. L. Johnson, V. Izquierdo-Roca, *Acta Materialia* **2020**, *183* 1.

[31] A. Nalin Mehta, H. Zhang, A. Dabral, O. Richard, P. Favia, H. Bender, A. Delabie, M. Caymax, M. Houssa, G. Pourtois, W. Vandervorst, *Journal of Microscopy* **2017**, *268*, 3 276.

[32] T. Chattopadhyay, J. Pannetier, H. G. Von Schnering, *Journal of Physics and Chemistry of Solids* **1986**, *47*, 9 879.

[33] H. Nozaki, M. Onoda, M. Sekita, K. Kosuda, T. Wada, *Journal of Solid State Chemistry* **2005**, *178*, 1 245.

[34] A. R. Jayakrishnan, J. S. Kim, M. Hellenbrand, L. Marques, J. MacManus-Driscoll, J. Silva, *Materials Horizons* **2024**.

[35] J. Jiang, Y. Bitla, C.-W. Huang, T. H. Do, H.-J. Liu, Y.-H. Hsieh, C.-H. Ma, C.-Y. Jang, Y.-H. Lai, P.-W. Chiu, W.-W. Wu, Y.-C. Chen, Y.-C. Zhou, Y.-H. Chu, *Science Advances* **2017**, *3*, 6 e1700121.

[36] J. Y. Park, D. H. Lee, G. H. Park, J. Lee, Y. Lee, M. H. Park, *Nanotechnology* **2023**, *34*, 20 202001.

[37] Y. Jiang, E. Parsonnet, A. Qualls, W. Zhao, S. Susarla, D. Pesquera, A. Dasgupta, M. Acharya, H. Zhang, T. Gosavi, C.-C. Lin, D. E. Nikonov, H. Li, I. A. Young, R. Ramesh, M. L. W, *Nature materials* **2022**, *21*, 7 779.

[38] A. Fernandez, M. Acharya, H.-G. Lee, J. Schimpf, Y. Jiang, D. Lou, Z. Tian, L. W. Martin, *Advanced Materials* **2022**, *34*, 30 2108841.

[39] K. C. Kwon, Y. Zhang, L. Wang, W. Yu, X. Wang, I.-H. Park, H. S. Choi, T. Ma, Z. Zhu, B. Tian, C. Su, K. P. Loh, *ACS nano* **2020**, *14*, 6 7628.

[40] J. Kreisel, M. Alexe, P. A. Thomas, *Nature materials* **2012**, *11*, 4 260.

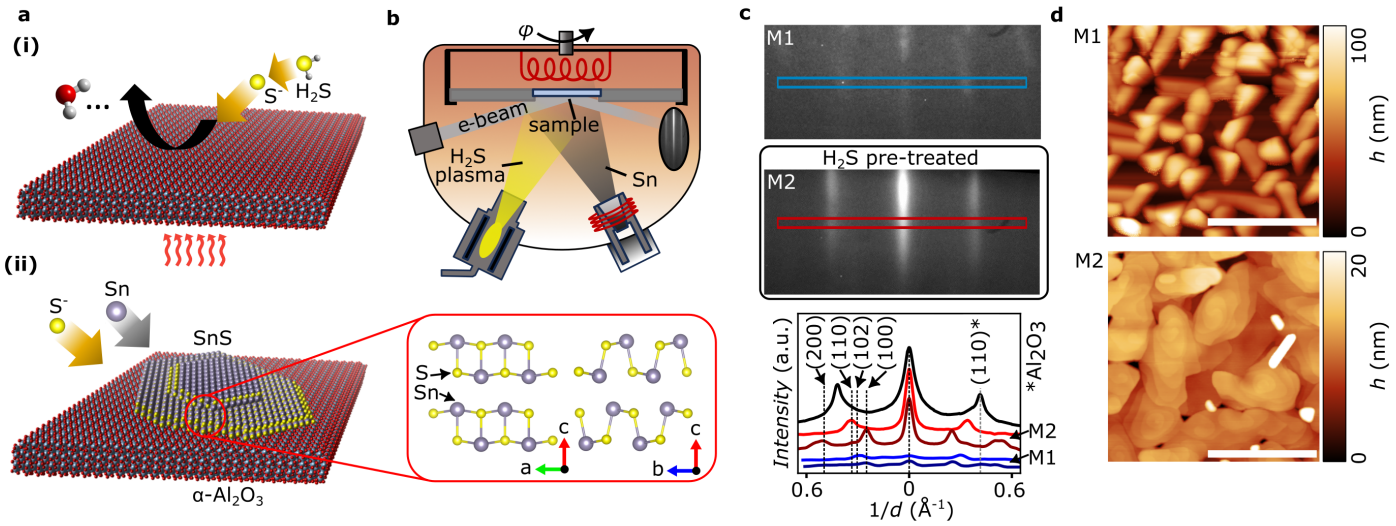

Figure 1: SnS growth process. a) Growth strategy involving high temperature H_2S plasma pre-treatment (i) followed by H_2S plasma assisted deposition (ii) resulting in basal plane SnS. b) Schematic of the growth chamber for PA-MBE. c) RHEED images of M2 vs M1. Taking the pattern of the α-Al_2O_3 substrate for calibration allows quantification of recipocal lattice spacing $1/d$ observed in M1 and M2 at different azimuth angles (see Supporting Info, Fig. S4). The intensity plot shows cuts of frames at two different azimuth angle for each, M1 and M2. Expected recipocal lattice spacings are indicated with dashed lines. d) Surface morphology of M1 (RMS=18.9 nm) vs M2 (RMS=3.6 nm) measured by AFM. Grains in M1 grow in distinct angles consistent with RHEED data (see Supporting Info, Fig. S3). Scale bar is 1 μm.

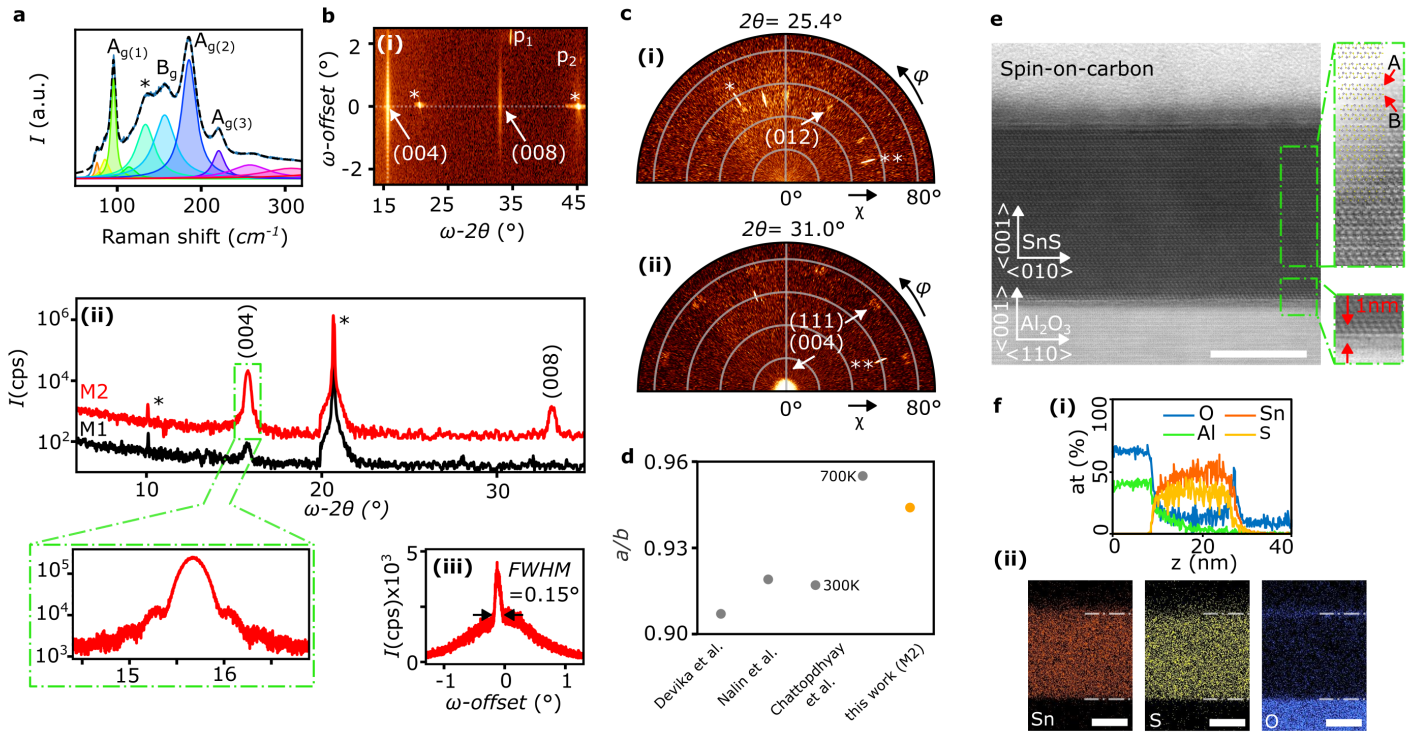

Figure 2: Structural characterization M2. a) Raman spectrum showing signature SnS peaks and an additional peak marked by * as discussed in the main text. b) (i) RSM of M2. The OOP scan (ii) and rocking curve (iii) correspond to cuts along the ω-offset= 0° and ω-2θ = 15.68° lines, respectively. The plotted intensity of M2 in (ii) is offset by a factor of 100 for clarity and substrate peaks are marked by *. c) Pole figures probing (i) SnS(102) and (ii) SnS(111) planes. d) comparison of a/b ratio with literature[18, 31, 32]. a/b of this work matches best with a high T value. Signal from the substrate and Si carrier wafer are marked with * and **, respectively. e) Cross section ABF-STEM image displaying the dislocation free, sharp interface of the AB stacked film with the substrate. f) (i) Elemental percentage profile and (ii) corresponding EDS maps across the film showing a homogeneous elemental distribution of Sn, S and O. All scale bars in f) and e) are 10 nm.

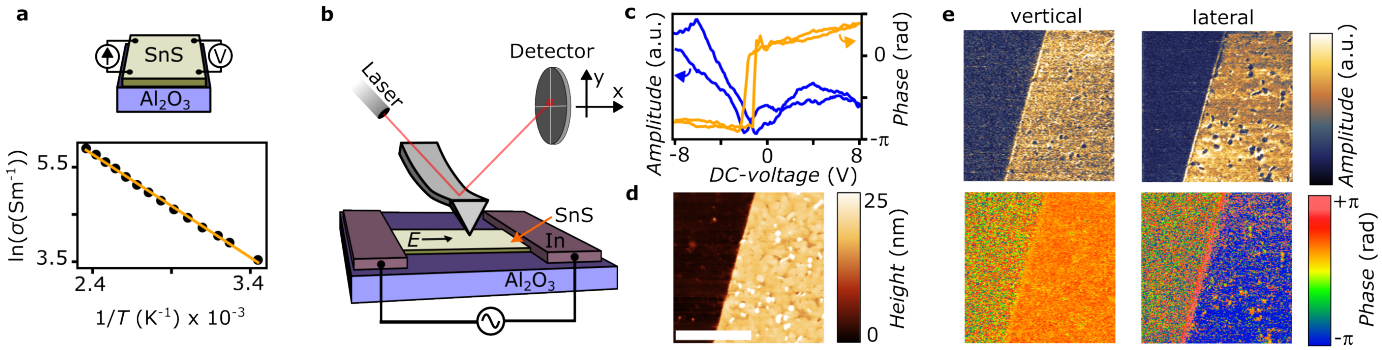

Figure 3: Sheet resistance and PFM in M2. a) σ as a function of $1/T$. A schematic of the used vdP geometry is shown above. b) Schematic of the in-plane PFM configuration. c) Sweep of the DC voltage offset applied to the In contacts and resulting vertical PFM amplitude and phase showing a small hysteresis. d) topographic map (scale bar is 2 μm). e) PFM amplitude and phase of the vertical and lateral deflection mapped over the edge of the film.

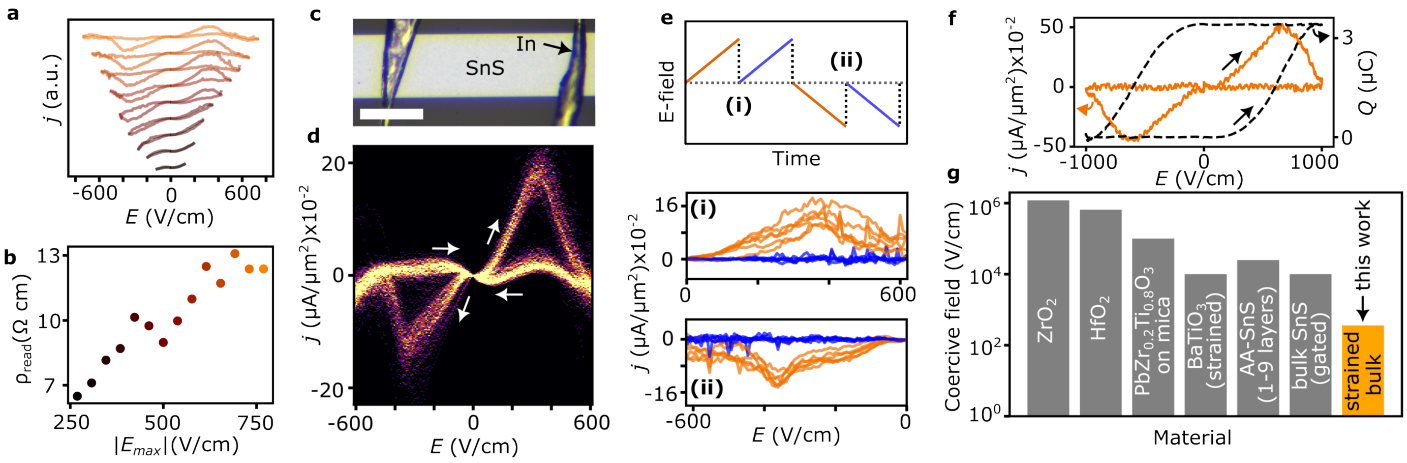

Figure 4: Memristive switching in thin film M2. a) IV curves recorded at incrementally increased applied electric field. b) Backtrace resistivity (measured at E_{read}=270 V/cm) in function of max field range in IV sweeps from a). c) Microscope image of the device. Scale bar is 50 μm. d) Overlay of 100 traces showing highly reproducible behaviour and switching fields of 360 V/cm. e) Repeated DWM by applying voltage according to the schematic on top (schematic shows one DWM cycle). The primary (orange) is clearly distinct from the secondary (blue) sweep by a high conductance peak. f) Simultaneous measurement of current and charge. The arrows indicate the direction of the voltage bias sweep. g) Comparison of switching fields of various material systems.

Table of Contents

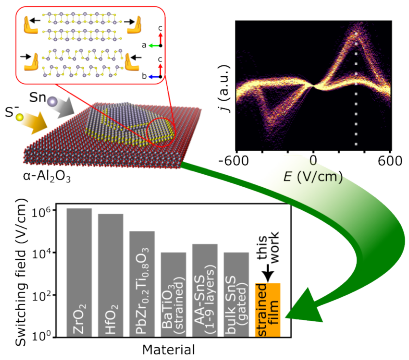

Tin monosulfide (SnS), a quasi-van der Waals ferroelectric semiconductor, shows promise for memristors, flexible photovoltaics, and piezoelectric devices. We achieve highly oriented SnS thin films on sulfur-pretreated α-Al_2O_3 substrates, combining chemical and physical growth. Induced in-plane strain breaks centrosymmetry, enabling stable, low-field (360 V/cm) memristive switching, advancing scalable, energy-efficient, adaptive electronics.

Supporting Info for: Low-Field Memristive Switching in Epitaxially Strained SnS Thin Film

System	SnS unit cell (AB)	single layer	multiple layers (AB, even)	multiple layers (AB, odd)	multiple layers (AA)
	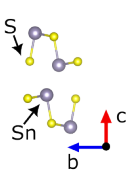	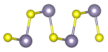	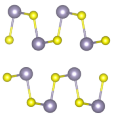	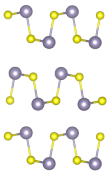	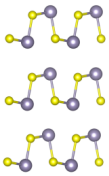
Centro-symmetry	yes	no	yes	no	no

Figure S1: Schematics of different stacking orders in SnS.

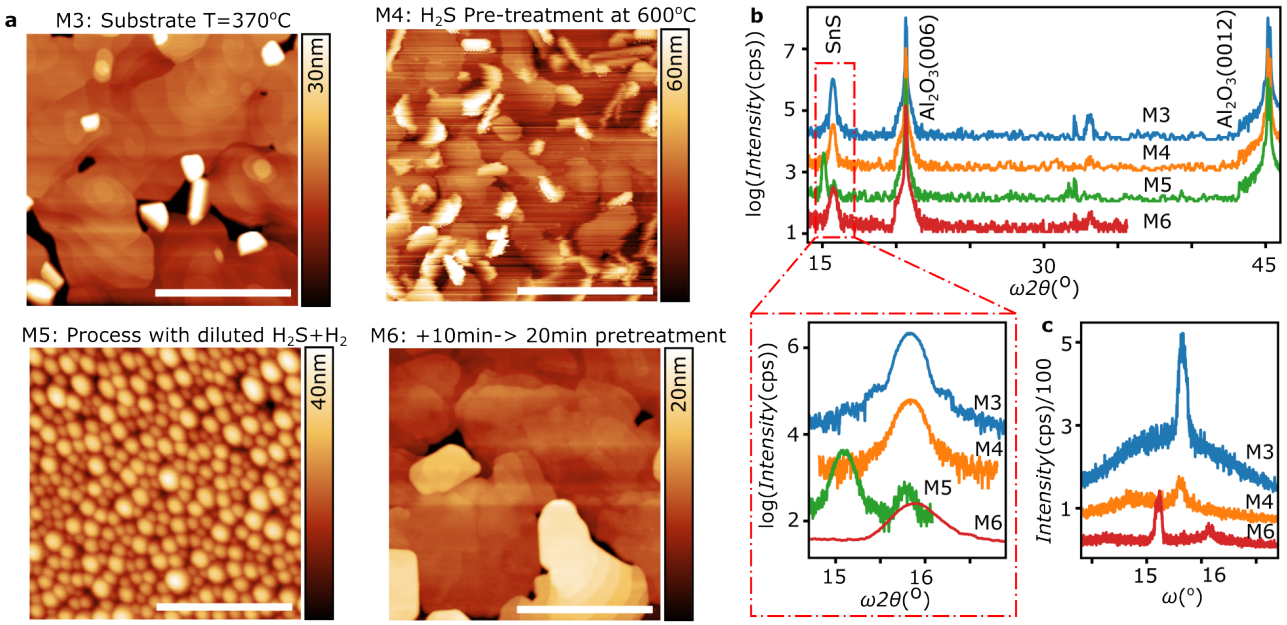

Figure S2: Comparison of various growth strategies for M3-M6 by AFM in a) and XRD in b). M3 shows the low impact of an additional 20°C added to the growth temperature of M2. M4 shows a high impact of executing the H_2S pre-treatment at 600°C, 150°C lower than for M2. M5 demonstrates a large morphology change when using H_2S diluted with H_2 for generating the plasma. M6 shows that adding 10min to the H_2S pre-treatment time leads to increased grain size. XRD scans on M3 are consistent with M2. M5 has two peaks at $\omega 2\theta$=15.1° and 15.8°, respectively. The first one can be assigned to SnS(111) and the second to SnS(004). c) XRD rocking curves on M3,4 and 6. The superposed sharp peak on M4 is significantly reduced compared to M2. On M6, it forms at a different ω angle. Scale bars in AFM images are 500 nm.

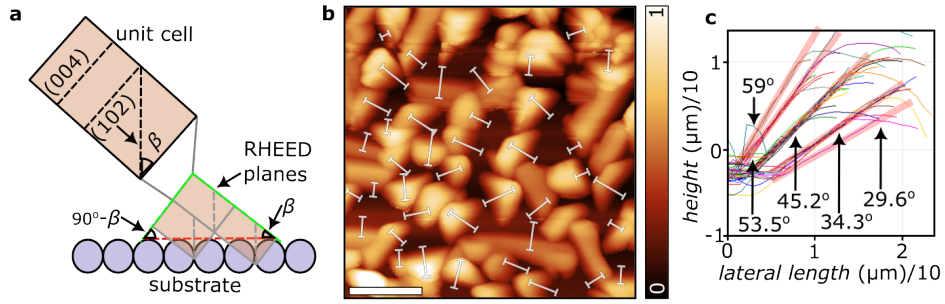

Figure S3: Grain angles measured on M1. a) Schematic of the relationship between planes measured by RHEED and angles observed in AFM. SnS(004) and SnS(102) are used as example. b) Topographic AFM image from main text overlaid with profile lines taken perpendicular to grain gradients. Scale bar is 250 nm. c) Collection of line profiles that align with five angles; 59.0°, 53.5°, 45.2°, 34.3° and 29.6°. Red areas represent average angles ±2° giving an error estimate of this method. SnS(004) and SnS(114) form an angle of 43.8° (90°-43.8°=46.2°) matching the most common angle. SnS(004) and SnS(102) form an angle of 54.9° and 90°-54.9°=35.1° matching well two of the most common observed angles consistent with RHEED data shown in the main text. SnS(004) and SnS(023) form 59.8° and 30.02° matching well with the two less common angles.

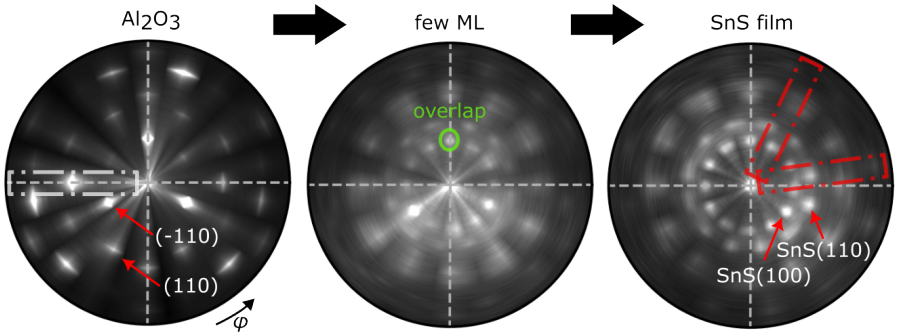

Figure S4: Polar RHEED scans of M2 showing in-situ the transition from substrate to film pattern. Grazing incidence RHEED polar figures are plotted by extracting line cuts for each frame during a azimuth rotation. Using this method to probe vertical planes allows to characterise the film texture in-situ. We observe a 12-fold symmetry corresponding to a 6-fold texture. By observing the transitional pattern at a few mono-layers (ML) we can estimate the epitaxial relation of the film with the substrate within resolution limited by the frame rate. In this case we get Al_2O_3(1-10)||SnS(100) at 360°/40 frames which agrees with the TEM data shown in the main text. Marked areas correspond to line profiles shown in main text.

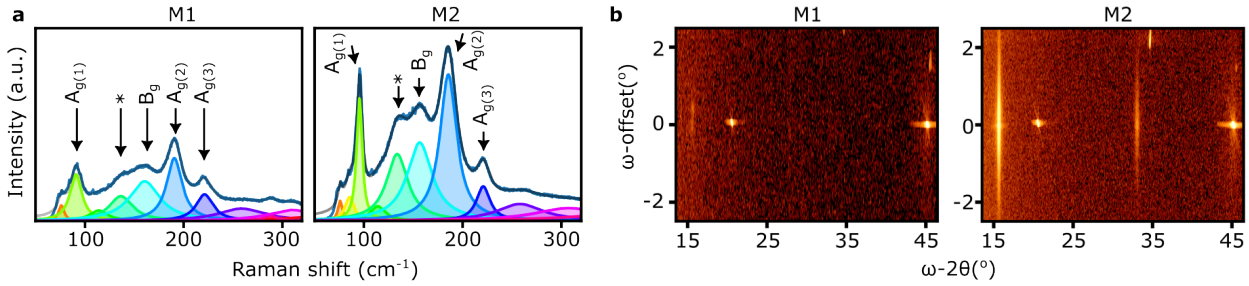

Figure S5: Comparison of M1 and M2 in Raman and XRD maps. a) Peak positions are ($A_{g(1)}$, *, B_g, $A_{g(2)}$, $A_{g(3)}$)= (90.9, 136.4, 160.5, 190.6, 221.2) cm^{-1} and (95.4, 133.6, 156.4, 185.4, 220.8) cm^{-1} for M1 and M2, respectively. Qualitatively, M1 and M2 produce the same Raman profile confirming that their difference is predominantly structural. Despite featuring a roughly equal amount of material, the general intensity is roughly 3 times larger in M2 confirming the superior crystallographic order. The peaks in M2 are diversely shifted in respect to M1 by a few cm^{-1}; red for $A_{g(1)}$ and blue for all others. This could be attributed to stress stemming from the differing growth mode and larger substrate interface. b) The off-axis peaks RSM are present in both samples but at different positions and intensities.

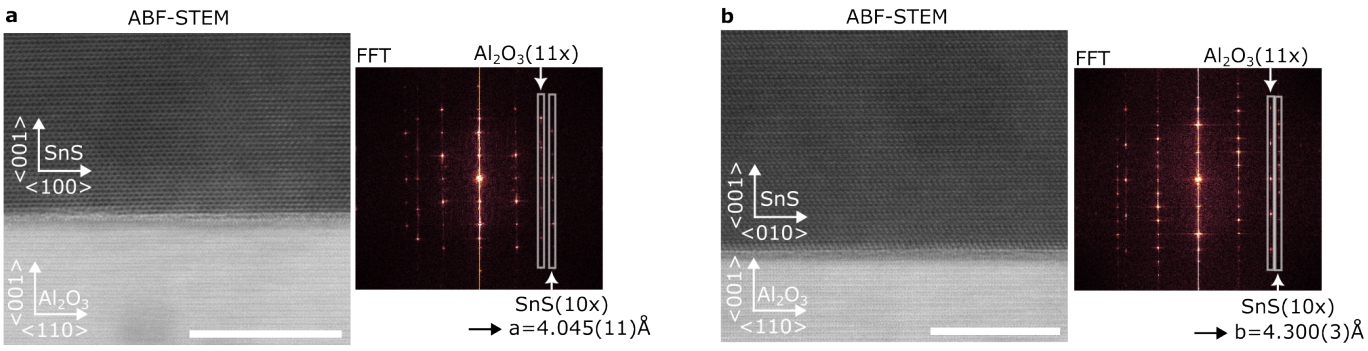

Figure S6: Cross sectional ABF-STEM images of the two main crystallographic in-plane directions in BP-SnS recorded from the same lamella of textured film M2. Lattice constants were extracted from the FFT images using the known lattice spacing of α-Al_2O_3(110), $d_{110}^{Al_2O_3}$=2.41$\AA$, yielding a^{SnS}=4.051$\AA$ in a) and b^{SnS}=4319$\AA$ in b). Scale bars are 10 nm.

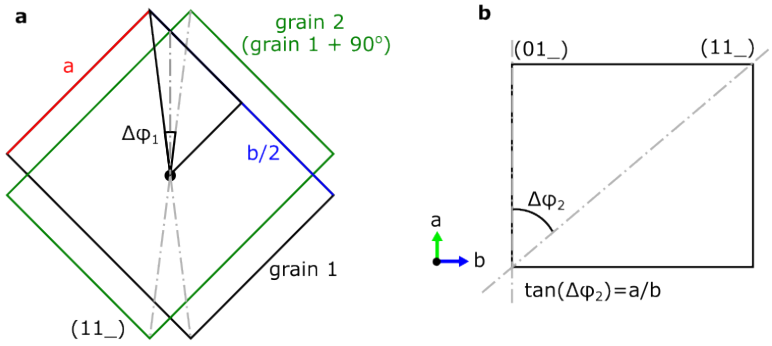

Figure S7: Geometry considerations relating XRD data to ratio a/b. a) $\Delta\phi_1$ between two perpendicular grains as measured in pole figures in the main text. c) $\Delta\phi_1$ is linked to a/b by b/a=tan(45°+$\Delta\phi_1$/2). b) $\Delta\phi_2$ between SnS(012) and SnS(111) planes which is directly related to a/b. The third index of (hkl) is accounted for by inclination around the polar angle χ and can be ignored in these considerations.

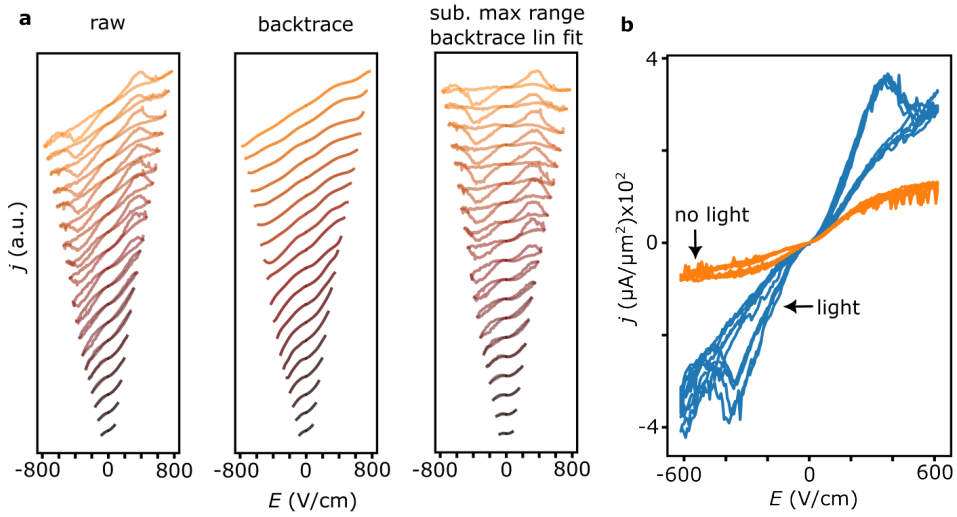

Figure S8: Background subtraction for IV curves recorded on the 2 terminal device shown in the main text. a) Exemplarily shows the processing steps applied to the transport data. We extract a linear background from the back-trace of curves recorded in the saturated switching regime, i.e. with a measurement range of 10V/130 μm. This linear background is subsequently extracted from curves of all ranges. The sample was exposed to the light of the microscope for all curves. b) We found a significant dependence of switching amplitude and overall current on light exposure. Here, we compare two loops with the microscope light turned on and off.

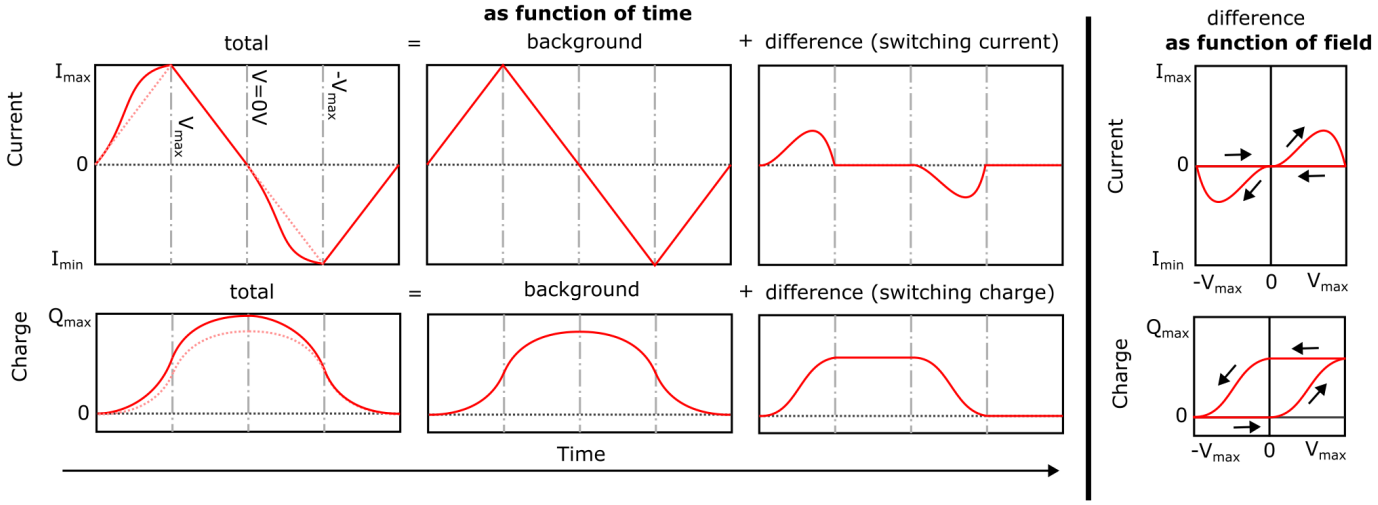

Figure S9: Background subtraction for the charge measurement. The schematic illustrates the process for a ohmic background which results in quadratic charge contributions. In the present analysis, non-linear background contributions have been accounted for by fitting a 4th order polynomial to the background.

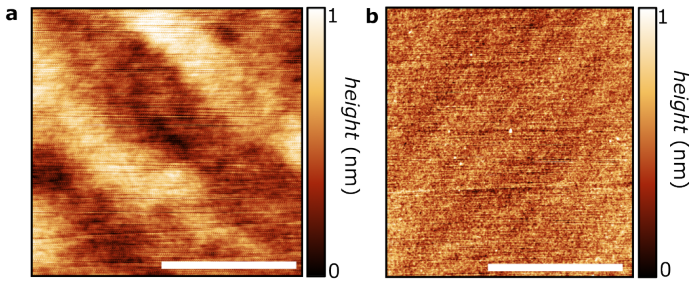

Figure S10: Comparison of a) pristine α-Al_2O_3(001) (RMS=194 pm) and b) α-Al_2O_3 pretreated by exposure to 500 W H_2S plasma for 10 min at substrate temperature of 600°C (RMS=158 pm). Scale bars are 1 μm.

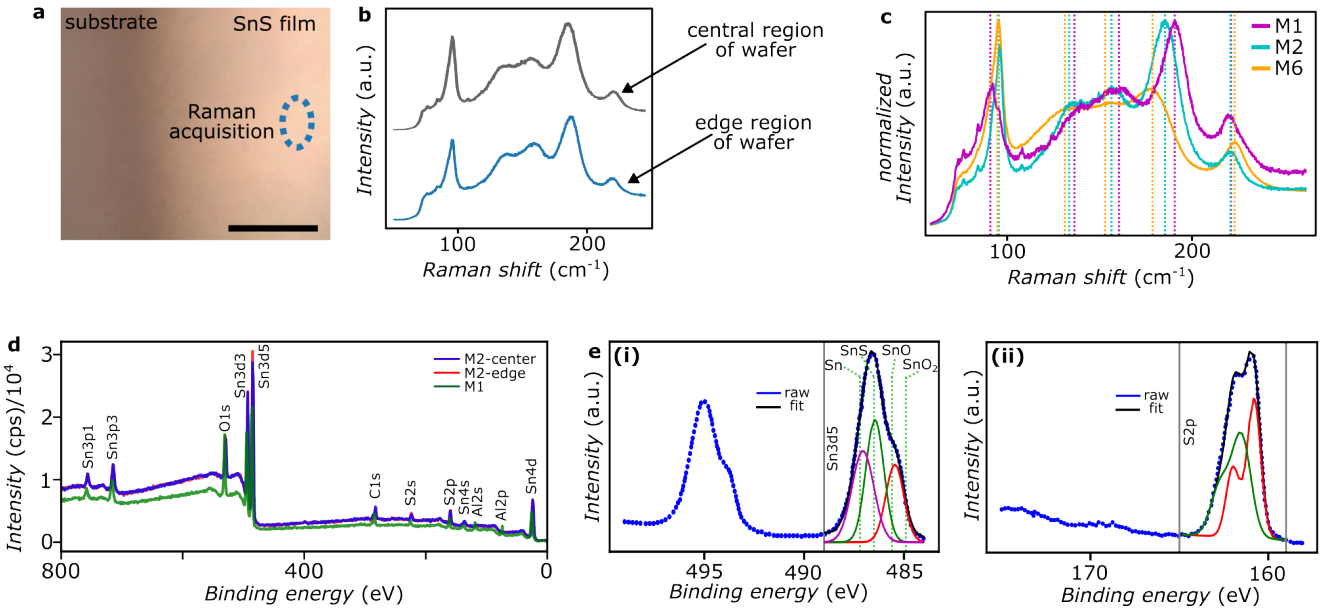

Figure S11: Confirmation of chemical uniformity of the SnS thin film and Raman comparison of M1, M2 and M6. a) Microscope image of the edge region of the wafer. Scale bar is 20 μm. b) Comparison of Raman spectra obtained at the central region of the film (shown in main text) and the edge region (highlighted in a)). c) The Ag(1) mode is blue shifted in M2 M6 compared to M1. Ag(2) and Bg modes are red shifted in M2 M6 compared to M1 (more for M6 which has roughly half of M2's film thickness). These observations are coherent with strain as the primary cause for inter-sample Raman shift differences. Intensities have been normalized to aid visual comparison. d) large range XPS survey scan comparing M1 and edge/center of the wafer in M2. e) detailed XPS scans of (i) Sn3d5 and (ii) S2p signal on M2. We attribute the three Sn3d5 peaks to SnS, SnO and SnO_2 at the surface of the film (see also Figure 2 f). The dotted lines in (i) indicate values from literature (M. Fondell, M. Gorgoi, M. Boman, A. Lindblad, Journal of Electron Spectroscopy and Related Phenomena 2014, 195 195). The two doublets observed in the S2p spectrum in (ii) are separated by 0.93 eV. This can be attributed to bulk/surface coordination differences (G. Von Oertzen, S. Harmer, W. Skinner, Molecular Simulation 2006, 32, 15 1207). XPS spectra were recorded using a monochromatized photon beam with 1486.6 eV and spot size of 100 μm.